Supporting Information for "Constraints from exhumed rocks on the seismic signature of the deep subduction interface"

C. M. Tewksbury-Christle[1], W. M. Behr[1]

[1]Structural Geology and Tectonics Group, Geological Institute, Department of Geosciences, ETH Zurich, Sonneggstrasse 5, 8092 Zurich, Switzerland

Contents of this file

1. Text S1 to S2
2. Figures S1 to S3
3. Tables S1 to S5

Introduction

This supporting information consolidates equations, detailed assumptions and results, and additional figures for calculating the seismic signature of a fossil subduction interface shear zone. Texts S1 and S2 contain equations for empircal and theoretical calculations for seismic velocities in fractured isotropic and anisotropic media. We used the MATLAB Seismic Anisotropy Toolbox (MSAT) to calculate the effect of mineral anisotropy and briefly discuss how we merged fracture and mineral anisotropy calculations in MSAT.

Tables S1 to S5 contain values calculated as described in the main text and further detailed in Texts S1 and S2.

Text S1. *Assumptions and calculations for fractured isotropic media.* Table S4 lists fracture characteristics measured for the CMS averaged across outcrop- and/or thin section-scale. Aspect ratio (α) and the crack density parameter (ϵ) were calculated as:

$$\alpha = \frac{aperture}{length} \tag{1}$$

$$\epsilon = \frac{3\phi}{4\pi\alpha} \tag{2}$$

Where ϕ is the porosity and the geometrical factor in the crack density parameter comes from the assumption of elliptical cracks.

We used the fracture characteristics in one empirical (Peacock et al., 2011) and two theoretical (O'Connell & Budiansky, 1974; Hudson, 1981) solutions for seismic wave velocities in fractured media, where Peacock et al. (2011)'s equation is:

$$\frac{V_P}{V_S} = 0.036\phi^2 + 0.0178\phi + 1.79 \tag{3}$$

Calculation of velocities for saturated elliptical cracks follows O'Connell and Budiansky (1974)'s equations (13) and (A3). Because of dependence of their T parameter on both aspect ratio (α) and effective Poisson's ratio ($\bar{\nu}$), we assumed an aspect ratio given in Table S4, solved for a range of effective Poisson's ratios, and selected the effective Poisson's ratio that corresponded to our calculated crack density parameters. Seismic velocities are calculated from the effective E and G of the fractured matrix with the following equations:

$$\frac{\bar{E}}{E} = 1 - \frac{16}{45}\left(1 - \bar{\nu}^2\right) T\epsilon \tag{4}$$

$$\frac{\bar{G}}{G} = 1 - \frac{8}{15}\left(1 - \bar{\nu}\right) T\epsilon \tag{5}$$

$$\epsilon = \frac{45}{8}\frac{\left(\bar{\nu} - \nu\right)}{\left(1 - \bar{\nu}^2\right)\left(1 - 2\nu\right) T} \tag{6}$$

Where E and G are the Young's and shear moduli of the matrix, respectively, and are output by the Abers and Hacker (2016) MATLAB toolbox, and $\bar{E}$ and $\bar{G}$ are the effective moduli of the fractured media. ν is the Poisson's ratio of the matrix (from Abers & Hacker, 2016) and $\bar{\nu}$ is the effective Poisson's ratio of the fractured media. ϵ is the crack density parameter. T is defined as follows:

$$T\left(\alpha, \bar{\nu}\right) = k^2 A \left[\frac{1}{\left(k^2 - \bar{\nu}\right) A + \bar{\nu}\alpha^2 B} + \frac{1}{\left(k^2 - \bar{\nu}\alpha^2\right) A + \bar{\nu}\alpha^2 B}\right] \tag{7}$$

where:

$$k = \left(1 - \alpha^2\right)^{1/2} \tag{8}$$

$$A = \int_0^{\pi/2} \left(1 - k^2 \sin^2\theta\right)^{1/2} d\theta \tag{9}$$

$$B = \int_0^{\pi/2} \left(1 - k^2 \sin^2 \theta\right)^{-1/2} d\theta \tag{10}$$

We calculated seismic velocities using the effective Poisson's ratio, Young's modulus, and density.

$$V_p = \sqrt{\frac{\bar{E}}{\bar{\rho}} \frac{(1-\bar{\nu})}{(1-2\bar{\nu})(1+\bar{\nu})}} \tag{11}$$

$$V_s = \sqrt{\frac{\bar{E}}{\bar{\rho}} \frac{1}{2(1+\bar{\nu})}} \tag{12}$$

For oriented fractures (Fig. S2) using the Hudson (1981) derivation, we used built-in MSAT functions. We derived an effective isotropic stiffness tensor from the individual lithologies to form the matrix and calculated water seismic velocities at CMS P-T conditions using Burnham, Holloway, and Davis (1969) thermodynamic properties.

$$V_p = \sqrt{\frac{K_{water} + \frac{4}{3}G}{\rho_{water}}} \tag{13}$$

$$K_{water} = 1/\kappa \tag{14}$$

$$G_{water} = 0 \tag{15}$$

$$\rho_{water} = V^{-1} \tag{16}$$

$$V = \left(\frac{\delta G}{\delta P}\right)_{T,n} \tag{17}$$

$$\kappa = -V^{-1}\left(\frac{\delta^2 G}{\delta P^2}\right)_{T,n} = -V^{-1}\left(\frac{\delta V}{\delta P}\right)_{T,n} \tag{18}$$

where K_{water} and ρ_{water} are the bulk modulus (Pa) and density of water (kg/m^3), V is the specific volume of water (m^3/kg), G is the Gibb's Free Energy of water, and P is the pressure (Pa). All values are calculated at 450 °C and 1 GPa. Fracture fill characteristics are: V_P = 2.22 km/s, V_S = 0 km/s, ρ = 1030 kg/m^3.

Detailed results in Table S5.

Text S2. *Assumptions and calculations for fractured anisotropic media.* To calculate the cumulative effect of fractures and anisotropic lithologies in MSAT, we decomposed the bulk stiffness tensor (calculated using MSAT and assumed mineral orientations, see Fig. S1) into isotropic and anisotropic components using the following steps and built-in MSAT functions:

1. Rotated anisotropic stiffness tensor to optimal orientation

2. Decomposed anisotropic stiffness tensor (C_{ijkl}) into C_{iso} + C_{hex} + C_{tet} + C_{ort} + C_{mon} + C_{tri}

3. Rotated C_{iso} and C_{aniso} back into primary orientation, where C_{aniso} = C_{hex} + C_{tet} + C_{ort} + C_{mon} + C_{tri}

We applied the Hudson (1981) formulation in MSAT to C_{iso} (required by MSAT calculations) and then summed $C_{iso\ +\ frac}$ and C_{aniso}.

References

Abers, G. A., & Hacker, B. R. (2016). A MATLAB toolbox and Excel workbook for calculating the densities, seismic wave speeds, and major element composition of minerals and rocks at pressure and temperature. *Geochemistry, Geophysics, Geosystems*, *17*(2), 616–624.

Audet, P., Bostock, M. G., Christensen, N. I., & Peacock, S. M. (2009). Seismic evidence for overpressured subducted oceanic crust and megathrust fault sealing. *Nature*, *457*(7225), 76–78.

Audet, P., & Bürgmann, R. (2014). Possible control of subduction zone slow-earthquake periodicity by silica enrichment. *Nature*, *510*(7505), 389–392.

Audet, P., & Schaeffer, A. J. (2018). Fluid pressure and shear zone development over the locked to slow slip region in Cascadia. *Science advances*, *4*(3).

Audet, P., & Schwartz, S. Y. (2013). Hydrologic control of forearc strength and seismicity in the Costa Rican subduction zone. *Nature Geoscience*, *6*(10), 852–855.

Burnham, C. W., Holloway, J. R., & Davis, N. F. (1969). *Thermodynamic Properties of Water to 1,000° C and 10,000 Bars*. Geological Society of America.

Calkins, J. A., Abers, G. A., Ekström, G., Creager, K. C., & Rondenay, S. (2011). Shallow structure of the Cascadia subduction zone beneath western Washington from spectral ambient noise correlation. *Journal of Geophysical Research: Solid Earth*, *116*(B7).

Delph, J. R., Levander, A., & Niu, F. (2018). Fluid controls on the heterogeneous seismic characteristics of the Cascadia margin. *Geophysical Research Letters*, *45*(20), 11–021.

Fukao, Y., Hori, S., & Ukawa, M. (1983). A seismological constraint on the depth of basalt–eclogite transition in a subducting oceanic crust. *Nature*, *303*(5916), 413–415.

Hansen, R. T., Bostock, M. G., & Christensen, N. I. (2012). Nature of the low velocity zone in Cascadia from receiver function waveform inversion. *Earth and Planetary Science Letters*, *337*, 25–38.

Hudson, J. A. (1981). Wave speeds and attenuation of elastic waves in material containing cracks. *Geophysical Journal International*, *64*(1), 133–150.

Kato, A., Iidaka, T., Ikuta, R., Yoshida, Y., Katsumata, K., Iwasaki, T., ... Hirata, N. (2010). Variations of fluid pressure within the subducting oceanic crust and slow earthquakes. *Geophysical Research Letters*, *37*(14).

Kato, A., Saiga, A., Takeda, T., Iwasaki, T., & Matsuzawa, T. (2014). Non-volcanic seismic swarm and fluid transportation driven by subduction of the Philippine Sea slab beneath the Kii Peninsula, Japan. *Earth, Planets and Space*, *66*(1), 1–8.

Kim, Y., Abers, G. A., Li, J., Christensen, D., Calkins, J., & Rondenay, S. (2014). Alaska Megathrust 2: Imaging the megathrust zone and Yakutat/Pacific plate interface in the Alaska subduction zone. *Journal of Geophysical Research: Solid Earth*, *119*(3), 1924–1941.

Kim, Y., Clayton, R., & Jackson, J. (2010). Geometry and seismic properties of the subducting Cocos plate in central Mexico. *Journal of Geophysical Research: Solid Earth*, *115*(B6).

Kodaira, S., Iidaka, T., Kato, A., Park, J.-O., Iwasaki, T., & Kaneda, Y. (2004). High pore fluid pressure may cause silent slip in the Nankai Trough. *Science*, *304*(5675),

1295–1298.

Matsubara, M., Obara, K., & Kasahara, K. (2009). High-V_p/V_s zone accompanying non-volcanic tremors and slow-slip events beneath southwestern Japan. *Tectonophysics*, *472*(1-4), 6–17.

O'Connell, R. J., & Budiansky, B. (1974). Seismic velocities in dry and saturated cracked solids. *Journal of Geophysical Research*, *79*(35), 5412–5426.

Peacock, S. M., Christensen, N. I., Bostock, M. G., & Audet, P. (2011). High pore pressures and porosity at 35 km depth in the Cascadia subduction zone. *Geology*, *39*(5), 471–474.

Toya, M., Kato, A., Maeda, T., Obara, K., Takeda, T., & Yamaoka, K. (2017). Down-dip variations in a subducting low-velocity zone linked to episodic tremor and slip: a new constraint from ScSp waves. *Scientific reports*, *7*(1), 1–10.

Tsuji, Y., Nakajima, J., & Hasegawa, A. (2008). Tomographic evidence for hydrated oceanic crust of the Pacific slab beneath northeastern Japan: Implications for water transportation in subduction zones. *Geophysical Research Letters*, *35*(14).

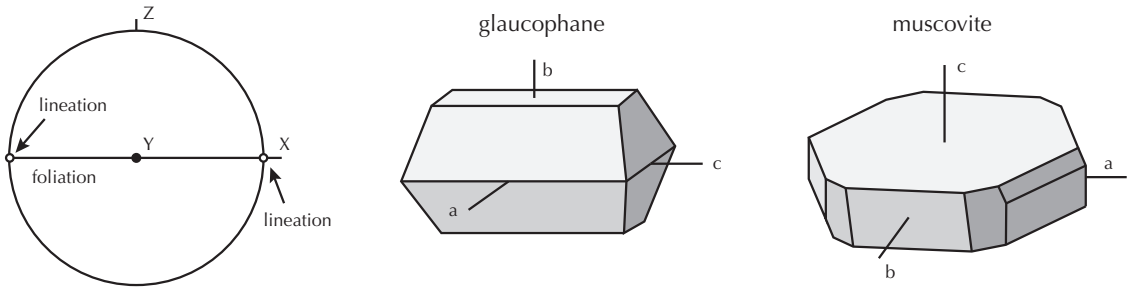

Figure S1. Assumed orientations for seismically anisotropic minerals that show evidence of crystallographic preferred orientations.

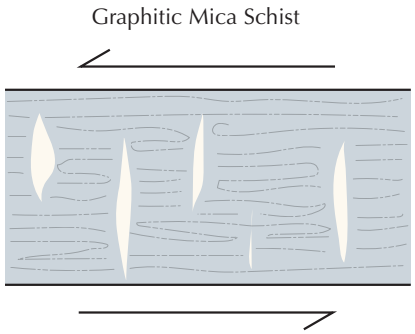

Figure S2. Assumed fracture orientations.

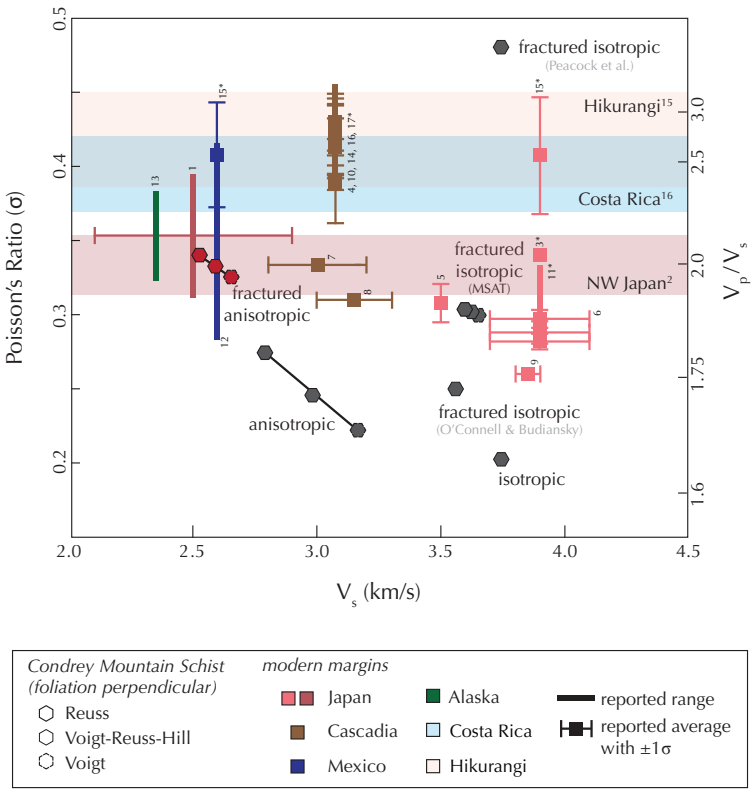

Figure S3. Comparison of V_p/V_s and V_s measured in modern subduction zones (Toya et al. (2017)[1], Tsuji et al. (2008)[2], Kodaira et al. (2004)[3], Hansen et al. (2012)[4], Kato et al. (2010)[5], Matsubara et al. (2009)[6], Delph et al. (2018)[7], Calkins et al. (2011)[8], Fukao et al. (1983)[9], Audet and Schaeffer (2018)[10], Kato et al. (2014)[11], Kim et al. (2010)[12], Kim et al. (2014)[13], Audet et al. (2009)[14], Audet and Bürgmann (2014)[15], Audet and Schwartz (2013)[16], Peacock et al. (2011)[17]) and calculated from the CMS assuming isotropic, anisotropic, fractured isotropic, and fractured anisotropic lithologies. All citations marked with an asterisk (*) are plotted with V_s values constrained by other studies for the same margin. Where V_s values are not available for a given margin, V_p/V_s is plotted as a color block.

Table S1. Volume fractions of minerals in individual CMS lithologies estimated as areal proportions assuming no significant anisotropy in the third dimension.

Lithology	Quartz	White Mica	Epidote	Glaucophane	Antigorite
Schist	0.3	0.7	-	-	-
Mafic Blueschist	0.05	0.05	0.30	0.60	-
Serpentinized Ultramafic	-	-	-	-	1

Table S2. Volume fractions of lithologies in the CMS estimated from structural thicknesses and assuming no significant anisotropy in the second or third dimensions.

Schist	Mafic Blueschist	Serpentinized Ultramafic
0.94	0.06	-

Table S3. Seismic velocities calculated at a range of P-T conditions using the Abers and Hacker (2016) MATLAB toolbox and assuming isotropic lithologies.

P-T	V_P	V_S	V_P/V_S
273.15 K, 101.3 kPa	6.22	3.80	1.64
0.8-1.0 GPa, 350-450 °C	6.18 - 6.20	3.74 - 3.76	1.64 - 1.65

Table S4. Porosities, aspect ratios, and crack density parameters measured for the schist.

Porosity	Aspect Ratio	Crack Density Parameter
%, ϕ	α	ϵ
10 ± 1	0.15	0.16

Table S5. Seismic velocities for different assumptions of shear zone anisotropy. Values for all calculations using MSAT are foliation-perpedicular.

Case	V_P (km/s)	V_{S1} (km/s)	V_{S2} (km/s)	$V_S{}^{avg}$ (km/s)	V_P/V_S	Method
Anisotropic	5.15	3.02	2.94	2.99	1.73	MSAT
Fractured isotropic	-	-	-	-	5.16	Peacock et al. (2011)
Fractured isotropic	6.15	-	-	3.57	1.71	O'Connell and Budiansky (1974)
Fractured isotropic	6.79	3.92	3.33	3.63	1.87	Hudson (1981), MSAT
Fractured anisotropic	5.14	3.09	2.06	2.58	2.00	Hudson (1981), MSAT